ACS OMEGA

http://pubs.acs.org/journal/acsodf

Article

Antimonene-Coated Uniform-Waist Tapered Fiber Optic Surface Plasmon Resonance Biosensor for the Detection of Cancerous Cells: Design and Optimization

Vikas and Paola Saccomandi*

Cite This: *ACS Omega* 2023, 8, 4627−4638

Read Online

ACCESS | Metrics & More | Article Recommendations

ABSTRACT: For early-stage cancer detection, a novel design of graphene-antimonene-coated uniform-waist tapered fiber optic surface plasmon resonance (SPR) biosensor is demonstrated. The proposed optical biosensor outperforms over a wide range of refractive index (RI) variations including biological solutions and is designed to detect various cancerous cells in the human body whose RIs are in the range of 1.36−1.4. Here, antimonene is used to enhance the performance of the designed SPR sensor for sensing cancer analytes because of its high binding energy toward adsorption of biomolecules and large active surface area. The design and analysis of the sensor are done with the help of a transfer matrix method-based simulation platform, and the effect of the taper ratio is also studied. The performance of the proposed SPR biosensor is evaluated with performance parameters such as sensitivity, full width at half maximum, detection accuracy (DA), figure of merit (FOM), and limit of detection (LOD). The numerical results show that the designed sensor is able to provide a sensitivity of 7.3465, 10.9250, 11.8914, and 15.2414 μm/RIU, respectively, for sensing skin, cervical, blood, and adrenal gland cancer with a maximum FOM of 131.1525 RIU^{-1}, DA of 14.2126 μm^{-1}, and LOD of 7.2 × 10^{-5} RIU. Based on the derived results, the authors believe that the designed SPR sensor could practically find its potential applications in the field of medical science for the early-stage diagnosis of cancer and hence, opens a new window in the field of biosensing.

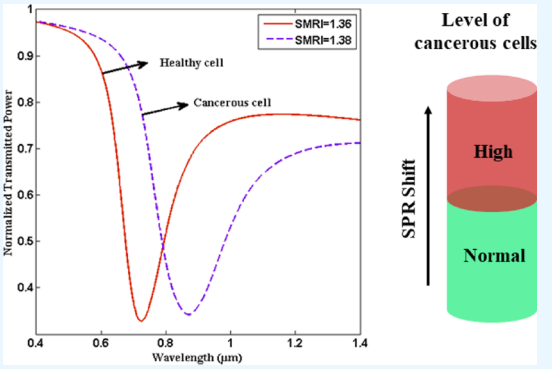

1. INTRODUCTION

Nowadays, rapid and real-time analysis of cancerous cells is a hot topic in the field of medical science. The fundamental abnormality resulting in the development of cancer is the continual unregulated proliferation of cancer cells.[1] Cancer has now become a serious concern for human health globally because of its high mortality rate.[2] As per World Health Organization reports, almost 10 million individuals were deceased due to cancer in 2020.[3] Among the different types of cancer, the most prominent are skin cancer (Basal cells), cervical cancer (HeLa cells), blood cancer (Jurkat cells), and adrenal gland cancer (PC12 cells). Basal cell carcinoma arises in the outer part of the epidermis due to excessive sun exposure and usually does not affect the other parts of the body.[4] HeLa is a cervical cancer cell line which grows uncontrollably and was the result of human papillomavirus infection in cervical cells.[5] A variation in the refractive index (RI) was observed when normal cells become cancerous. For example, healthy HeLa cells have an RI of 1.368, which increases to 1.392 when cancer develops. The RIs of various healthy and cancerous cells are presented in Table 1. Generally, the classification of cancer is categorized into three stages: Stage I, Stage II, and Stage III. Cancer-affected patients can be cured during Stages I and II, but the patients in Stage III cannot be cured. Thus, if the cancer cells in the affected area are not detected in the early stage, the cancer spreads to the other parts of the body leading to the death of the patient. Therefore, it is important to detect cancer at an

Table 1. RI Values for Healthy and Cancer-Affected Cells[6,7]

type of cancer	cell name and its concentration level	RI of healthy cell (concentration level 30−70%)	RI of cancer-affected cell
skin	Basal (80%)	1.36	1.38
cervical	HeLa (80%)	1.368	1.392
blood	Jurkat (80%)	1.376	1.39
adrenal gland	PC12 (80%)	1.381	1.395

Received: September 18, 2022
Accepted: December 5, 2022
Published: January 24, 2023

early stage for better treatment and saving the life of cancer patients.

Normally, blood tests (such as blood count, blood protein testing, cancer marker testing, etc.) and urine tests are performed to detect cancer, but the observed results could not clearly indicate the affected part of the body.[8] Biopsy is one of the best techniques to detect the cancerous cells present in different parts of the body.[9] Other popular methods such as electrochemical methods,[10] computed tomography,[11] immunocytochemistry,[12] magnetic resonance imaging,[13] Raman spectroscopy,[14] and microfluidic devices[15] have been employed to detect various cancerous cells. However, these methods are very complex and time-consuming which can lead to adverse effects for cancer-affected patients, requiring rapid diagnosis. Therefore, rapid and label-free sensing techniques are needed to differentiate among the normal and cancerous cells. Since healthy and cancerous cells possess different RIs, and hence, they have different propagation characteristics when exposed to light from the same source. In recent times, optical sensors have emerged as a powerful tool for accurate and real-time monitoring of cancerous cells at a lower cost than other detection methods.[4,16−19] In 2012, Yaroslavsky et al. experimentally presented a real-time noninvasive detection of Basal cell carcinomas using high contrast mapping.[4] Later on, a label-free detection of various cancerous cells was performed using the optical absorption-based technique.[16] In the same year, Ramanujam et al. theoretically investigated the detection of a cancer cell utilizing a one-dimensional nanocomposite material-coated photonic crystal and attained a maximum sensitivity of 43 nm/RIU.[17] After this, Sani and Khosroabadi presented the numerical analysis of an optical biosensor based on resonance cavities for the detection of blood component, diabetes, cancer, and glucose concentration.[18] The results showed that the highest sensitivities for detecting Basal cells, HeLa cells, diabetes, and MDA-MB-231 cells were observed to be 1500, 1250, 2333, and 1428 nm/RIU, respectively. Recently, Yasli theoretically designed a surface plasmon resonance (SPR)-based photonic crystal fiber biosensor for the detection of early-stage cancer, which exhibited a maximum sensitivity of 7142.86 nm/RIU.[19] The advancements in optical fiber technology have renovated the sensing capabilities of optical fiber-based sensing devices[20−22] and enhanced their use for biomedical applications in the oncological domain.[23,24] These devices have plenty of advantageous features such as resistance to electromagnetic interference, light weight, remote sensing applications, easy designing, capability of wavelength multiplexing, multiparameter measurements,[25] fast response time, and high sensitivity with a wide detection range.[26,27] Thus, by taking into consideration the several advantageous features accessible from optical fiber, the research area of fiber optic sensors is reached to a level where miniaturized low-cost devices are easily achievable for fast and consistent sensing applications. In this framework, prism/optical fiber-based sensors satisfy many of these valuable properties. The biggest drawback of the prism coupling technique is the relatively bulky nature of its components. On the other hand, optical sensors utilizing a fiber core as a substrate offer several advantages such as high sensitivity, low weight, and being easy to handle. Due to these valuable features, the fiber optic sensors are employed as a substitute of conventional optical sensors and, hence, can be used as an experimental tool to attain stable and precise measurements in research laboratory. In the past few years, the fiber optic sensors based on the SPR technique have gained substantial consideration in the field of sensing as they are effective in various sensing applications.[28−31] SPR is a surface-sensitive technique in which the wave vector matching condition of the surface plasmon wave (SPW) and evanescent wave (EW) causes the excitation of surface plasmons (SPs) at the metal-dielectric interface.[32] This is because the light propagating through optical fiber experiences attenuated total reflection (ATR) at the core−metal interface. At SPR conditions, the complete transfer of energy from EW to SPW takes place, which results in a sharp drop in the intensity of reflected light at resonance wavelength (RW). Any changes in the RI near the surface of the plasmonic material lead to the modification in the wave vector of the SPW, and hence, the resonance condition is satisfied at some another wavelength value. Numerically, the SPR condition can be described as

$$\frac{\omega}{c}\sqrt{\varepsilon_{\text{core}}}\sin\theta = \frac{\omega}{c}\sqrt{\frac{\varepsilon_{\text{m}}\varepsilon_{\text{s}}}{\varepsilon_{\text{m}}+\varepsilon_{\text{s}}}} \quad (1)$$

Here, the left-hand side represents the wave vector of the EW and right-hand side shows the wave vector of the SPW, and $\varepsilon_{\text{core}}$, ε_{m}, and ε_{s} are the dielectric constants of the fiber core, metal, and sensing medium, respectively. Numerous investigations have been carried out to enhance the performance of the SPR-based fiber optic sensors, such as single mode fiber,[33] multimode fiber,[34] U-shaped fiber,[35] D-shaped fiber,[36] tapered fiber,[37] and fiber grating sensor.[38] Out of them, tapering the fiber core provides better results for sensitivity enhancement.[39−41] Also, to make the fiber sensing probes capable of biosensing, a biorecognition layer such as graphene and antimonene is an essential requirement.

Recent investigations on SPR sensing illustrate that the deposition of 2-D materials (such as graphene, molybdenum disulfide, black phosphorus, $Ti_3C_2T_X$ MXene, tungsten disulfide, etc.) on a thin metallic film acts as a biorecognition material and greatly enhances the sensing performance of the designed SPR biosensors.[42−44] Some of the significant features of 2-D materials include a greater surface to volume ratio, better electrical conductivity, good water solubility, higher molecular adsorption efficiency, and the feasibility of immobilization of biomolecules on their surface.[45] For this purpose, we design a tapered fiber optic SPR biosensor by depositing a thin gold (Au) film over the fiber core which is then followed by the deposition of 2-D materials, such as graphene and antimonene, over it.

Graphene is a 2-D material formed by a single graphite layer in which the carbon atoms having sp^2 hybridization are arranged in a honeycomb lattice.[46] It possesses better optical, mechanical and electrical properties such as high charge carrier mobility (10^6 cm^2 V^{-1} s^{-1}),[46] bigger surface to volume ratio and a stable structure among graphene layers.[47] Benefiting from these excellent properties, graphene offers a strong adsorption of biotargets and provides higher molecular absorption efficiency.[48] These advantageous features make graphene a better sensing material with high sensitivity for its utilization in various sensing applications.[49−53]

Moreover, antimonene possesses better electrochemical properties, strong spin-orbit coupling, a larger work function, low thermal conductivity, better optical response, and higher stability than graphene and rest of the 2-D materials due to more delocalized 5s/5p orbitals.[54] It is shown that the bulk antimony has an sp^2 bonded honeycomb lattice structure

https://doi.org/10.1021/acsomega.2c06037
ACS Omega 2023, 8, 4627−4638

similar to the graphene. In 2019, Xue et al. proposed an ultrasensitive detection of microRNA using antimonene-coated SPR sensor.[55] More recently, Singh et al. theoretically designed an SPR biosensor for the detection of hemoglobin (Hb) concentration using a nanolayered structure of $BaTiO_3$ and antimonene.[56] The designed SPR sensor results in an RI sensitivity of 303.83 degree/RIU, a figure of merit (FOM) of 50.39 RIU^{-1}, and a resolution of 0.021 g/mL for Hb detection. In the upcoming section, a detailed methodology of the proposed tapered fiber structure and its utilization in RI sensing and cancerous cell detection are provided.

2. METHODOLOGY

2.1. Design Consideration and Theoretical Model of the Tapered Fiber Optic SPR Sensor. The schematic diagram of the proposed tapered fiber optic SPR biosensor for the detection of cancerous cells is depicted in Figure 1. The

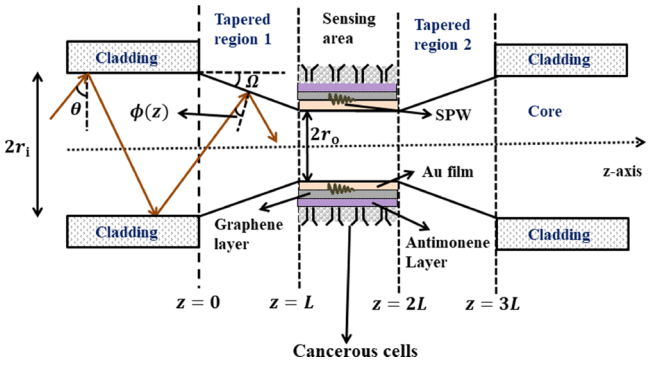

Figure 1. Schematic diagram of the proposed tapered fiber optic SPR biosensor.

sensing structure uses the Kretschmann−Raether configuration[32] realized on a step-index multimode optical fiber with a core diameter (D) of 600 μm and a numerical aperture of 0.24. Subsequently, a 0.5 cm length of the cladding is removed from the central part of the optical fiber using a sharp blade and this cladding-removed portion of the optical fiber can be tapered using the flame brush technique as described in ref 57.

In Figure 1, we can see that the proposed structure consists of three parts: a waist region (serves as a sensing region) with a small and uniform core diameter, and two identical tapered regions (namely Tapered region 1 and Tapered region 2) with a gradually expand diameter beside the uniform-waist region. Then, a thin film of Au having thickness 50 nm is deposited on the cladding etched part of the uniform fiber core to excite the SPs. This is because Au offers better chemical stability and enhanced sensitivity than other SPR-active materials, i.e., silver (Ag), copper (Cu), and aluminum (Al).[58] Furthermore, the monolayers of graphene and antimonene are coated on the Au film to improve the sensitivity and efficiency of the designed SPR biosensor due to better adsorption of biomolecules on it. This sensing layer is used to detect the various cancerous cells which act as the sensing medium. Thus, the sensing configuration of the proposed fiber optic SPR biosensor consists of five layers, i.e., fiber core/Au-film/graphene monolayer/antimonene monolayer/sensing medium. Experimentally, the fabricated fiber optic sensing probe can be fixed in a glass flowcell which is mounted on a 3-D translational stage.[31] After this, the different sensing samples can be injected into this glass flowcell such that the sensing medium comes in direct contact with the fabricated fiber optic sensing probe. Using a tungsten halogen light source, the light is launched from one of the ends of the optical fiber at an angle 'θ', and from another end, the light is spectrally investigated using an Avasoft spectrometer. The spectrometer is then further interfaced to a computer in which the transmission spectrum can be observed. Due to the phenomenon of ATR, the light propagates inside the fiber core and causes the multiple number of reflections inside it. After this, the guided rays of light enter the tapered region, and the angle of incidence 'θ' is transformed into 'ϕ (z)', which can be calculated as per equation given below[59]

$$\phi(z) = \cos^{-1}\left[\frac{r_i \cos\theta}{r(z)}\right] - \Omega \tag{2}$$

Here, '$2r_i$' and '$2r_o$' are the corresponding diameters of the fiber core at input and output ends of the taper respectively, and '$r(z)$' measures the radius of the fiber core at taper position 'z', and 'Ω' is the taper angle which can be written as

$$\Omega = \tan^{-1}\left(\frac{r_i - r_o}{L}\right) \tag{3}$$

where 'L' is the length of the sensing region. If the entire guided rays are launched into the optical fiber, then at the output end of the taper [i.e., $r(z) = r_o$], the angles θ_1 and θ_2 get converted into ϕ_1 and ϕ_2 which can be calculated using eq 2. Moreover, $\theta_1 = \sin^{-1}\left(\frac{n_{Au}}{n_{core}}\right)$ and $\theta_2 = \frac{\pi}{2}$, in which n_{core} and n_{Au} are the corresponding RIs of the optical fiber core and Au layer, respectively. Here, we introduce a new parameter, taper ratio (TR), which is defined as the ratio of the input core diameter to the output core diameter at taper ends, i.e., $\frac{2r_i}{2r_o}$.

2.2. Dispersion Properties. In the proposed structure, we have employed a wavelength interrogation scheme for numerical modeling of the tapered fiber optic SPR sensor, and therefore, we need to know the dispersion relation or dielectric constant of each layer. It is assumed that the fiber core is made of fused silica, and hence, wavelength dependency of its RI as per Sellmeier dispersion relation can be inscribed as[60]

$$n_{core}(\lambda) = \sqrt{1 + \frac{A_1\lambda^2}{\lambda^2 - B_1^2} + \frac{A_2\lambda^2}{\lambda^2 - B_2^2} + \frac{A_3\lambda^2}{\lambda^2 - B_3^2}} \tag{4}$$

Here, 'λ' is the wavelength of incident light in measured in μm, and A_1, A_2, A_3, B_1, B_2, and B_3 are the Sellmeier coefficients, and their numerical values are calculated as: A_1 = 0.6961663, A_2 = 0.4079426, A_3 = 0.8974794, B_1 = 0.0684043, B_2 = 0.1162414, and B_3 = 9.896161. The next layer is composed of Au, and its dispersion relation as per the Drude−Lorentz formula can easily be calculated as[58]

$$\varepsilon_{Au}(\lambda) = \varepsilon_r + i\,\varepsilon_i = 1 - \frac{\lambda^2\lambda_c}{\lambda_p^2(\lambda_c + i\,\lambda)} \tag{5}$$

Here, 'λ_c' and 'λ_p' denote the collision and plasma wavelengths, respectively, and their corresponding numerical values are 8.9342×10^{-6} and 1.6826×10^{-7} m. The next layer is made of graphene having a monolayer thickness of 0.34 nm, which gets coated over the Au film. The dispersion formula of the graphene layer is given by the following equation[61]

https://doi.org/10.1021/acsomega.2c06037
ACS Omega 2023, 8, 4627−4638

$$n_{\text{graphene}}(\lambda) = 3.0 + i\frac{K}{3}\lambda \tag{6}$$

where 'K' is a numerical constant and equals to 5.446 μm^{-1} and 'λ' is measured in μm. The fourth layer is composed of antimonene, having a monolayer of thickness 0.50 nm,[56] which gets deposited over the graphene layer. The RI of the antimonene monolayer comprising both real and imaginary parts can be obtained from the experimental results obtained by Ares et al.[62] in which the RI is related to its dielectric permittivity by the relation $n = \sqrt{\varepsilon}$ and its complex RI can be achieved by polynomial fitting as

$$n_{\text{Antimonene}}(\lambda) = n^{\text{real}}_{\text{Antimonene}} + i^{*}n^{\text{imaginary}}_{\text{Antimonene}} \tag{7}$$

where

$$n^{\text{real}}_{\text{Antimonene}} = x_0 + x_1{}^{*}\lambda + x_2{}^{*}\lambda^2 + x_3{}^{*}\lambda^3 + x_4{}^{*}\lambda^4 + x_5{}^{*}\lambda^5 \tag{8}$$

in which x_0 = 1959.24777, x_1 = −17.79855, x_2 = 0.0638, x_3 = -1.1264×10^{-4}, x_4 = 9.79905 $\times10^{-8}$ and x_5 = -3.36177×10^{-11} and

$$n^{\text{imaginary}}_{\text{Antimonene}} = p_0 + p_1{}^{*}\lambda + p_2{}^{*}\lambda^2 + p_3{}^{*}\lambda^3 + p_4{}^{*}\lambda^4 + p_5{}^{*}\lambda^5 \tag{9}$$

in which p_0 = 2201.26715, p_1 = −20.99288, p_2 = 0.07959, p_3 = -1.49746×10^{-4}, p_4 = = 1.39766×10^{-7}, and p_5 = -5.17482×10^{-11} and 'λ' is measured in nm.

At last, the fifth layer consists of the sensing analytes in the form of various cancerous cells such as Basal, HeLa, Jurkat, and PC12 whose concentration level is 80%, and for a healthy cell, the concentration level lies between 30 and 70%. The corresponding values are provided in Table 1. Before computing the numerical results for the cancerous cells, we have used a sensing medium refractive index (SMRI) of 1.333 because most biological/chemical samples are in aqueous form and the adsorption of any biomolecules will cause a variation in the SMRI. For this purpose, we have considered an altered value of the SMRI as 1.335 and also, the study is performed for a wide range of RI variations (1.33−1.37). The entire simulation in this study has been carried out using the latest version of MATLAB software.

2.3. Reflection Coefficient and Transmitted Power.

The calculation of reflectivity by means of the transfer matrix method in the form of the N-layer structure is the most precise, effective and does not require any approximation and thus, has been employed in the present study. In our proposed structure, we have number of layers as 5 i.e., N = 5.

In Figure 2, it is assumed that 'd_j' is the thickness, 'μ_j' is permeability, 'n_j' is the RI, and 'ε_j' is the permittivity of any arbitrary jth layer. If P_1, Q_1 and P_{N-1}, Q_{N-1} represent the tangential components of electric field ($\vec{E}$) and magnetic field ($\vec{B}$) at first and N_{th} boundary respectively, then they are correlated by the following relation

$$\begin{bmatrix} P_1 \\ Q_1 \end{bmatrix} = C\begin{bmatrix} P_{N-1} \\ Q_{N-1} \end{bmatrix} \tag{10}$$

Here, 'C' denotes the characteristic matrix for the p-polarized light of order 2 × 2 and can be written in the form of their matrix element as

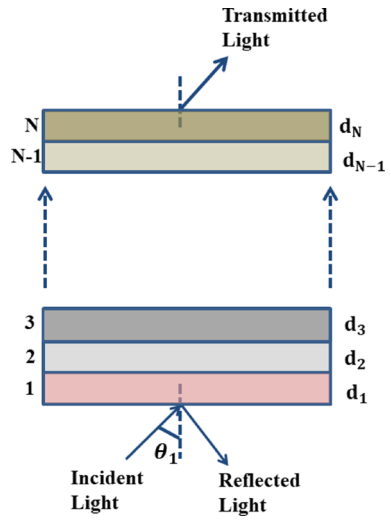

Figure 2. N-layer matrix model for the calculation of the reflection coefficient.

$$C = \prod_{j=2}^{N-1} C_j = \begin{bmatrix} C_{11} & C_{12} \\ C_{21} & C_{22} \end{bmatrix} \tag{11}$$

and

$$C_j = \begin{bmatrix} \cos\delta_j & (-i\sin\delta_j)/q_j \\ -iq_j\sin\delta_j & \cos\delta_j \end{bmatrix} \tag{12}$$

Here, 'q_j' and 'δ_j' measure the optical admittance and phase factor for each layer in the SPR biosensor, respectively, which are computed using the following equations

$$q_j = \left(\frac{\mu_j}{\varepsilon_j}\right)^{1/2}\cos\theta_j = \frac{(\varepsilon_j - n^2_{\text{core}}\sin^2\theta_1)^{1/2}}{\varepsilon_j} \tag{13}$$

and

$$\delta_j = \frac{2\pi}{\lambda}n_j\cos\theta_j(Z_j - Z_{j-1}) = \frac{2\pi d_j}{\lambda}(\varepsilon_j - n^2_{\text{core}}\sin^2\theta_1)^{1/2} \tag{14}$$

Here, θ_1 measures the angle made by the incident ray from normal to the j_{th} interface. Finally, using the matrix elements, the expression for reflection coefficient (r_p) becomes

$$r_p = \frac{(C_{11} + C_{12}q_N)q_1 - (C_{21} + C_{22}q_N)}{(C_{11} + C_{12}q_N)q_1 + (C_{21} + C_{22}q_N)} \tag{15}$$

Moreover, the reflectivity of a p-polarized light is attained by

$$R_p = |r_p|^2 \tag{16}$$

Furthermore, the energy distribution of each mode in the fiber satisfies the equation given below:

$$P(\theta) = \frac{n^2_{\text{core}}\sin\theta\cos\theta}{(1 - n^2_{\text{core}}\cos^2\theta)^2} \tag{17}$$

To calculate the effective transmitted power, the reflectivity (R_p) for a solo-reflection is raised to the power of number of reflections (N_{ref}). In addition, the beam of all modes satisfies the Fresnel equation.[63] Therefore, the total transmitted power in the proposed tapered fiber structure is attained by

https://doi.org/10.1021/acsomega.2c06037
ACS Omega 2023, 8, 4627−4638

integrating the beams of all modes, and the generalized expression for normalized transmitted power is obtained as:

$$P_{trans} = \frac{\int_{\phi_1}^{\phi_2} R_p^{N_{ref}(\theta)} P(\theta) d\theta}{\int_{\phi_1}^{\phi_2} P(\theta) d\theta} \quad (18)$$

where '$N_{ref}(\theta)$' measures the number of reflections and can be expressed as

$$N_{ref}(\theta) = \frac{L}{2r_o \tan(\theta + \Omega)} \quad (19)$$

Also, the formula for the amplitude of reflection coefficient (r_p) in terms of its output phase (ϕ_p) can be expressed as

$$r_p = |r_p| e^{i\phi_p} \quad (20)$$

2.4. Performance Parameters. For the designed SPR biosensor, the performance is evaluated in terms of its performance parameters such as sensitivity, detection accuracy (DA), full width at half maximum (FWHM), FOM, and limit of detection (LOD). For a typical transmitted SPR curve, the minimum value of transmission is obtained at a specific wavelength also known as RW, i.e., λ_R, which is very sensitive with a small variation in the SMRI. These performance parameters are described below one by one.

2.4.1. Sensitivity (S). It is demarcated as the ratio of shift in RW, i.e., $\delta\lambda_R$ to the change in the SMRI, i.e., δn_s. Here, sensitivity is measured in the units of μm/RIU, and the corresponding mathematical formula will be

$$S = \frac{\delta\lambda_R}{\delta n_s} \quad (21)$$

2.4.2. Full Width at Half Maximum. It is obtained by measuring the FWHM of the transmitted SPR curve. It is measured in the units of μm and mathematically can be written as

$$\text{FWHM} = \delta\lambda_{0.5} \quad (22)$$

2.4.3. Detection Accuracy. It is also known as the signal to noise ratio (SNR) which inversely depends on the FWHM and is given by

$$\text{DA} \propto \frac{1}{\text{FWHM}} \quad (23)$$

2.4.4. Figure of Merit. It is defined as the ratio of sensitivity to the FWHM and measured in the units of RIU^{-1}. The mathematical formula for the FOM can be written as

$$\text{FOM} = \frac{S}{\text{FWHM}} \quad (24)$$

2.4.5. Limit of Detection. It quantitatively measures the concentration of biomolecules in the sensing medium and is numerically defined as

$$\text{LOD} = \frac{\Delta\lambda}{S} \quad (25)$$

Here, '$\Delta\lambda$' measures the wavelength resolution of the used spectrometer which is considered as 0.00110 μm in our case. The LOD is measured in the units of refractive index unit (RIU). In the next section, we will explain the numerical results obtained for the designed tapered fiber optic SPR biosensor.

3. NUMERICAL RESULTS AND DISCUSSION

In recent times, the monolayer and multilayers of 2-D materials have already been deposited on the metal surface.[64]

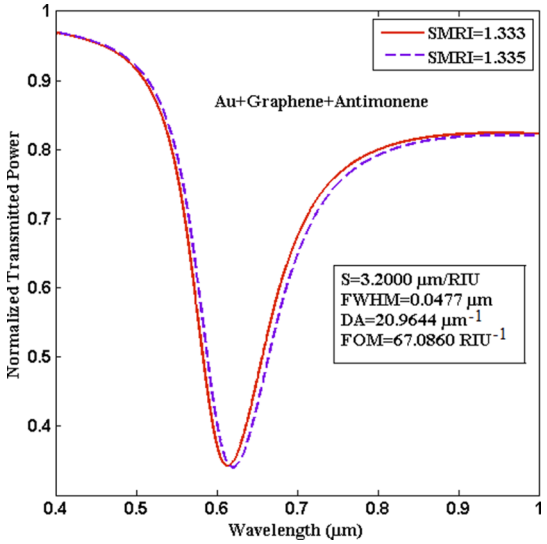

Figure 3. Transmitted SPR spectra for the proposed fiber sensing configuration at TR 1.0.

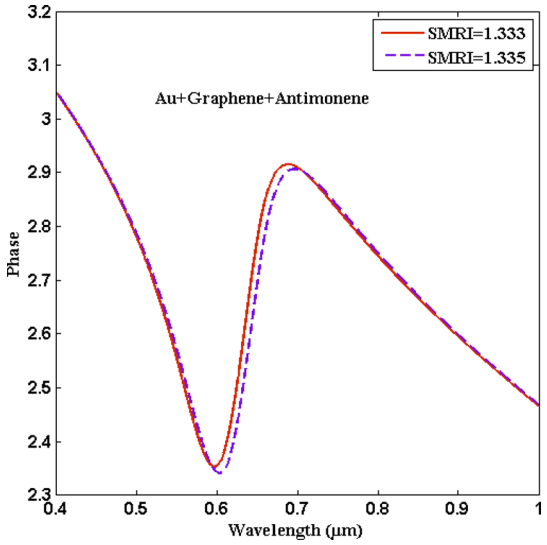

Figure 4. Variation of the output phase with wavelength for the proposed sensing configuration.

Thus, with the use of existing coating procedures, the deposition of monolayer antimonene over the graphene-metal surface can be easily done, and hence, the fabrication of the antimonene-coated fiber optic SPR biosensor proposed in this work is practically achievable. To explore the advantageous features of antimonene in RI sensing and in cancerous cell detection, the design of uniform-waist tapered fiber optic SPR sensor using MATLAB software is numerically investigated. In the designed tapered structure, it should be considered that Tapered region 1 is used to bring the incident angle values closer to the critical angle and Tapered region 2 allows the incident rays to regain their original values. In our

https://doi.org/10.1021/acsomega.2c06037
ACS Omega 2023, 8, 4627−4638

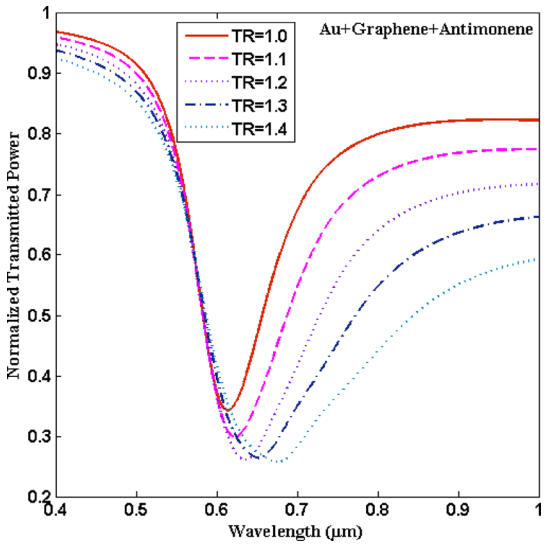

Figure 5. Effect of the taper ratio on transmitted SPR spectra for the proposed sensing configuration.

simulation, we have considered Au as an SPR-active material and thus gets coated over the uniform-waist fiber core placed between two equally tapered regions. The Au film is then coated with the additional layers of graphene-antimonene, and the effect of these overlayers is described in the upcoming section.

3.1. Effect of Graphene-Antimonene Overlayers. Figure 3 depicts the transmitted SPR spectra for the proposed fiber sensing configuration (Au + graphene + antimonene) at TR 1.0, i.e., the untapered core. It is noted that for a particular value of SMRI, i.e., 1.333, a minimum in the spectrum is achieved at an RW of 0.6136 μm. If we increase the SMRI by an amount of 0.002 RIU, the RW is shifted to 0.6200 μm, showing a redshift of 0.0064 μm in the RW. The reason for this change in the RW can be explained from eq 1 as follows: if we increase the SMRI, there will be a change in the RI of the SPW and hence, the resonance condition will be satisfied at some higher wavelength value, resulting a shift in RW. Also, the shift in RW is more in the present case, when compared with the fiber sensing configuration having only the Au film.

The corresponding value of sensitivity, FWHM, DA, and FOM at TR 1.0 comes out to be 3.2 μm/RIU, 0.0477 μm, 20.9644 μm^{-1}, and 67.0860 RIU^{-1}, respectively. A possible reason for the increase in sensitivity could be the work function of Au (5.1 eV) which is higher than that of graphene (4.5 eV) and antimonene (4.59 eV). This causes the effective transfer of electrons from graphene-antimonene overlayers to the Au-surface by the process of optical excitation. This method generates a larger electric field at the sensing interface which is responsible for the sensitivity enhancement. Furthermore, the coating of graphene-antimonene over the Au film enhances the light absorption of the Au-graphene-antimonene structure, and therefore, the electric field so raised results in a stronger SPR excitation. One can also see that the transmitted SPR spectra lie in the visible-near IR regime, which means that the proposed sensor works well in this wavelength region of the EM spectrum.

The elucidation of the SPR mechanism can also be understood in terms of the phase variation of the SPR output signal. If the output phase of the reflected light instead of transmitted power is measured, a robust resonant dip in the phase spectra is detected. Thus, it becomes imperative to provide the more evidence of the SPR sensing mechanism in terms of its phase variation, as fabrication of these multilayered fiber structures mainly depends on the phase change mechanism.[65] Figure 4 shows the behavior of the output phase of the reflected light as a function of the wavelength for two different SMRIs. It is observed that the output phase of the reflected light vicissitudes dramatically near the excitation point of SPR and like the transmitted SPR spectrum, a shift in the RW is achieved with the increase in the SMRI. In the next section, the effect of the TR on performance of the designed SPR sensor is discussed.

3.2. Effect of Tapering. Figure 5 illustrates the transmitted SPR spectra of the proposed fiber sensing configuration for various TRs. One can observe that if we increase the TR with a step size of 0.1, the RW shifts to higher values and the broadening of curves can also be seen. It was also noticed that an increase of more than 1.4 in the TR results in distorted

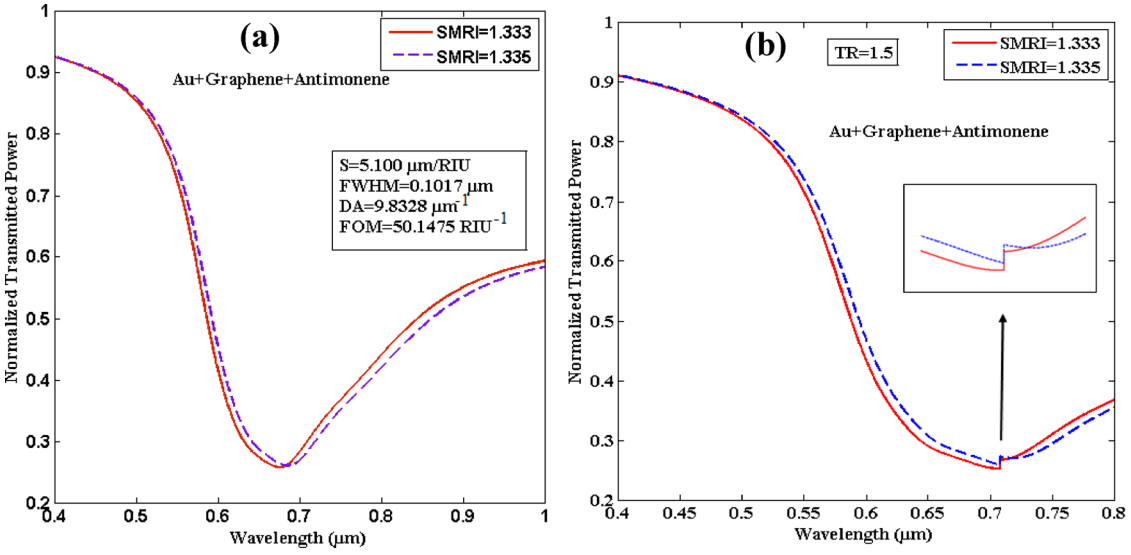

Figure 6. Transmitted SPR spectra for the proposed configuration at (a) TR 1.4 and (b) TR 1.5.

https://doi.org/10.1021/acsomega.2c06037
ACS Omega 2023, 8, 4627−4638

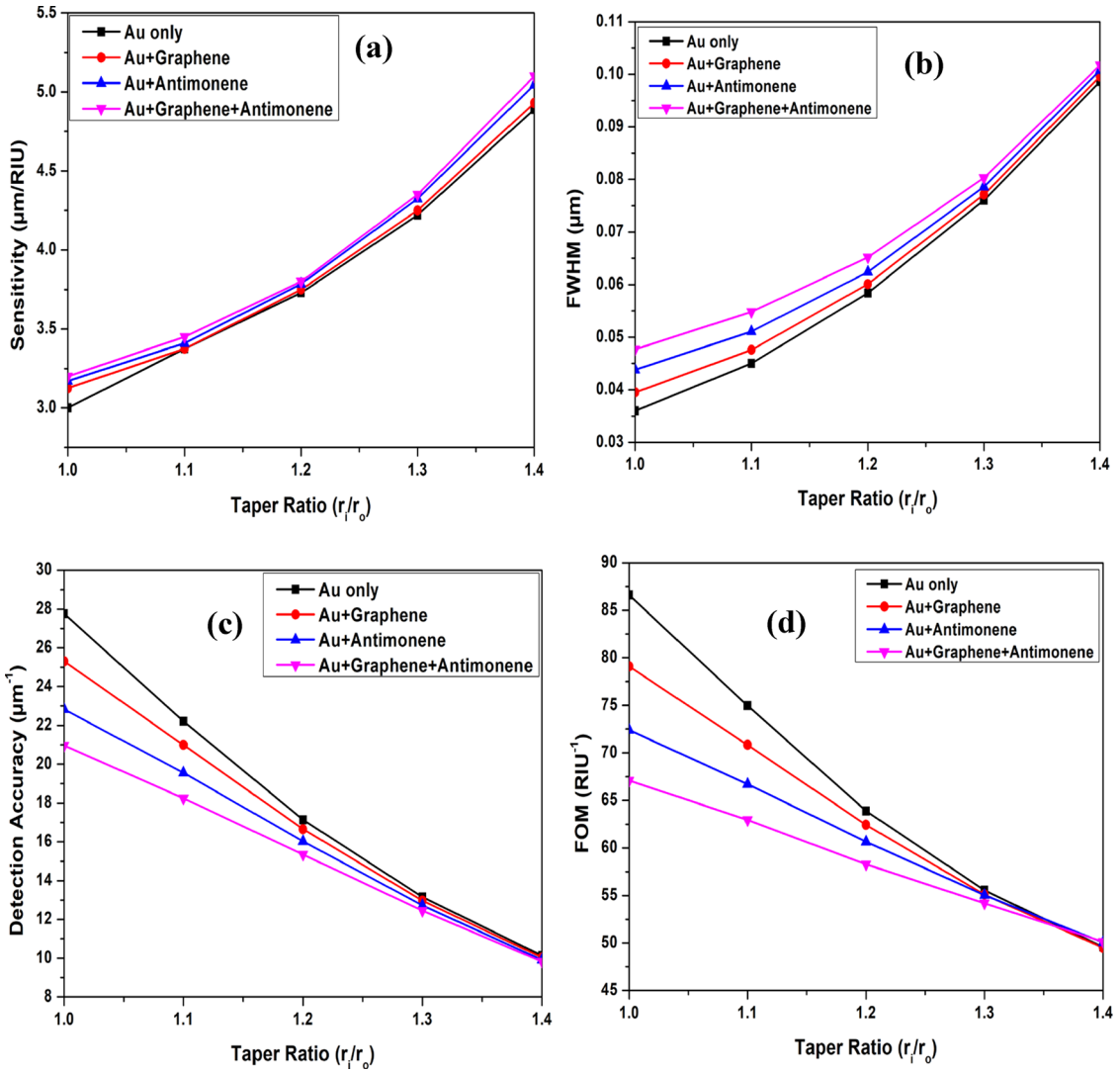

Figure 7. Variation of (a) sensitivity, (b) FWHM, (c) DA, and (d) FOM, for different fiber sensing configurations at various taper ratios.

transmitted SPR spectra and thus, the RW cannot be measured experimentally (as shown in Figure 6b).

Therefore, the optimized value of TR is 1.4 in our present case, and for the same reason, we have calculated the performance parameters of the designed sensor up to 1.4. Figure 6a displays the transmitted SPR spectra of the proposed fiber sensing configuration at a TR of 1.4. From the numerical results, we observed that for two different SMRIs, i.e., 1.333 and 1.335, the RW comes out to be 0.6751 and 0.6853 μm, respectively. It results in a sensitivity of 5.1 μm/RIU at a TR of 1.4 for the designed fiber configuration which is enhanced up to 59% on comparing the results achieved at a TR of 1.0. This improvement in the sensitivity can be described as follows: with Tapered region 1, the angle of bounded rays in the fiber core becomes closer to the critical angle. This can be attained by selecting the smallest diameter of the fiber core at the taper end due to which the whole bounded rays will propagate within the sensing area. After passing the sensing area, the rays will arrive in Tapered region 2, which transforms the angle of these bounded rays to their initial values to obtain the complete bounded rays at the output end of the fiber core. If we choose the smallest value of the core diameter, then no ray will come out from the sensing area and a major number of rays will propagate with angle closer to that of the critical angle. Thus, the EW will penetrate with a larger penetration depth and will result in a strong coupling of EW with the SPW that leads to the higher sensitivity in the case of the proposed structure.

As discussed earlier, the SPR curves become wider with the increase in the TR and hence a higher value of FWHM. This broadening in transmitted SPR curves may be due to the increase in electron energy loss which was stated for graphene.[66] At a TR of 1.4, the FWHM was increased to 0.1017 μm, which is higher than the value at a TR of 1.0 (0.0477 μm). As DA and FOM depend inversely on the FWHM, therefore, their values decrease with the increase in the TR. Consequently, the DA and FOM come out to be 9.8328 μm^{-1} and 50.1475 RIU^{-1}, respectively. In the next section, we will analyze and compare the performance of various fiber sensing configurations.

3.3. Performance Comparison of Various Fiber Sensing Configurations. To further extend the study, we consider four different sensing configurations: Au-only, Au + graphene, Au + antimonene, and Au + graphene + antimonene and then, we calculate and compare the performance parameters for these configurations. Figure 7a–d show the

https://doi.org/10.1021/acsomega.2c06037
ACS Omega 2023, 8, 4627−4638

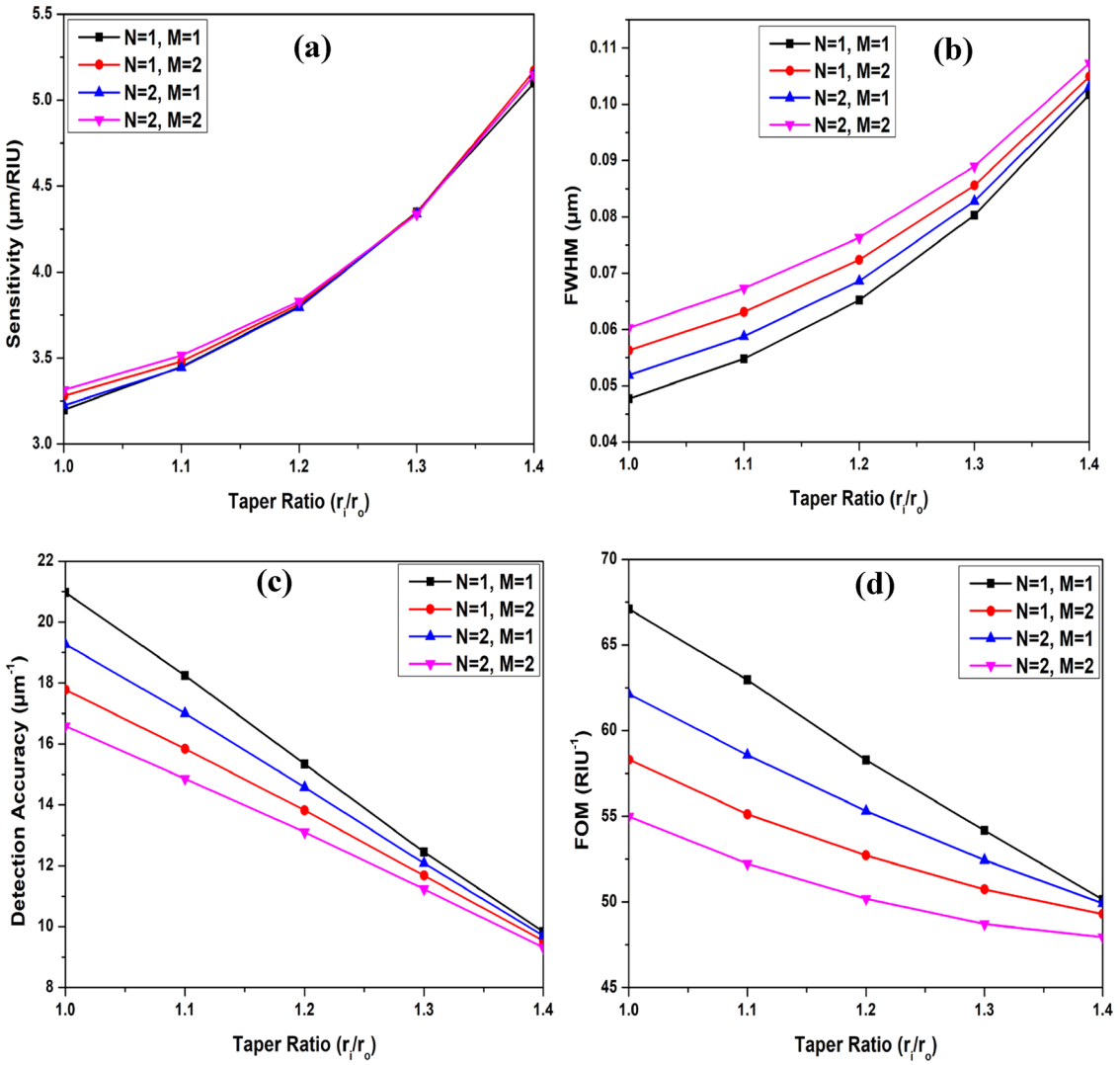

Figure 8. Variation of (a) sensitivity, (b) FWHM, (c) DA, and (d) FOM, with the increase in the number of graphene and antimonene overlayers at various taper ratios.

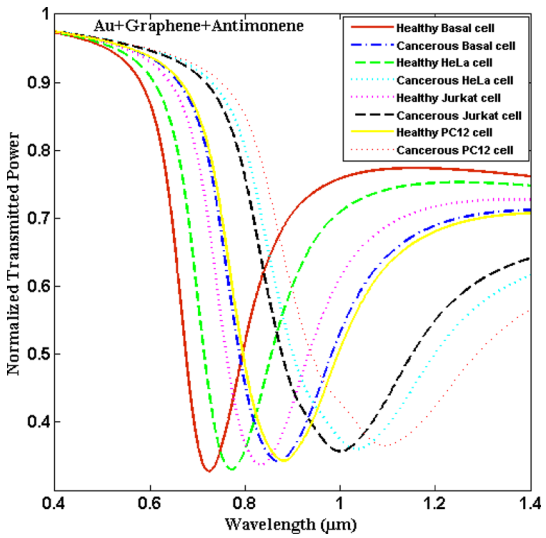

Figure 9. Transmitted SPR curves for the various types of healthy and cancerous cells.

variation of sensitivity, FWHM, DA, and FOM with TR for different fiber sensing configurations. From Figure 7a, we observed that sensitivity increases with the increase in TR for each configuration up to TR 1.4. However, sensitivity values are higher for the Au + graphene + antimonene configuration, then followed by Au + antimonene, Au + graphene, and Au-only configurations. Similarly, FWHM values raise with the increase in the TR for each configuration and are maximum for Au + graphene + antimonene configuration as shown in Figure 7b. On the other hand, DA and FOM values decrease with the increase in the TR for each configuration as depicted in Figure 7c,d, respectively. The maximum values of DA and FOM are achieved for Au-only and minimum for the Au + graphene + antimonene configuration. In the next section, we will observe the effect of increasing the number of layers of 2-D materials on the performance of the proposed SPR sensor.

3.4. Effect of Increasing the Number of Graphene and Antimonene Overlayers. Recent studies suggest that the performance of the SPR sensors based on 2-D materials also depends on the number of layers of these materials.[60] Therefore, in the present study, we have investigated the effect of increasing the number of monolayers of graphene and antimonene on sensitivity, FWHM, DA, and FOM for the

https://doi.org/10.1021/acsomega.2c06037
ACS Omega 2023, 8, 4627−4638

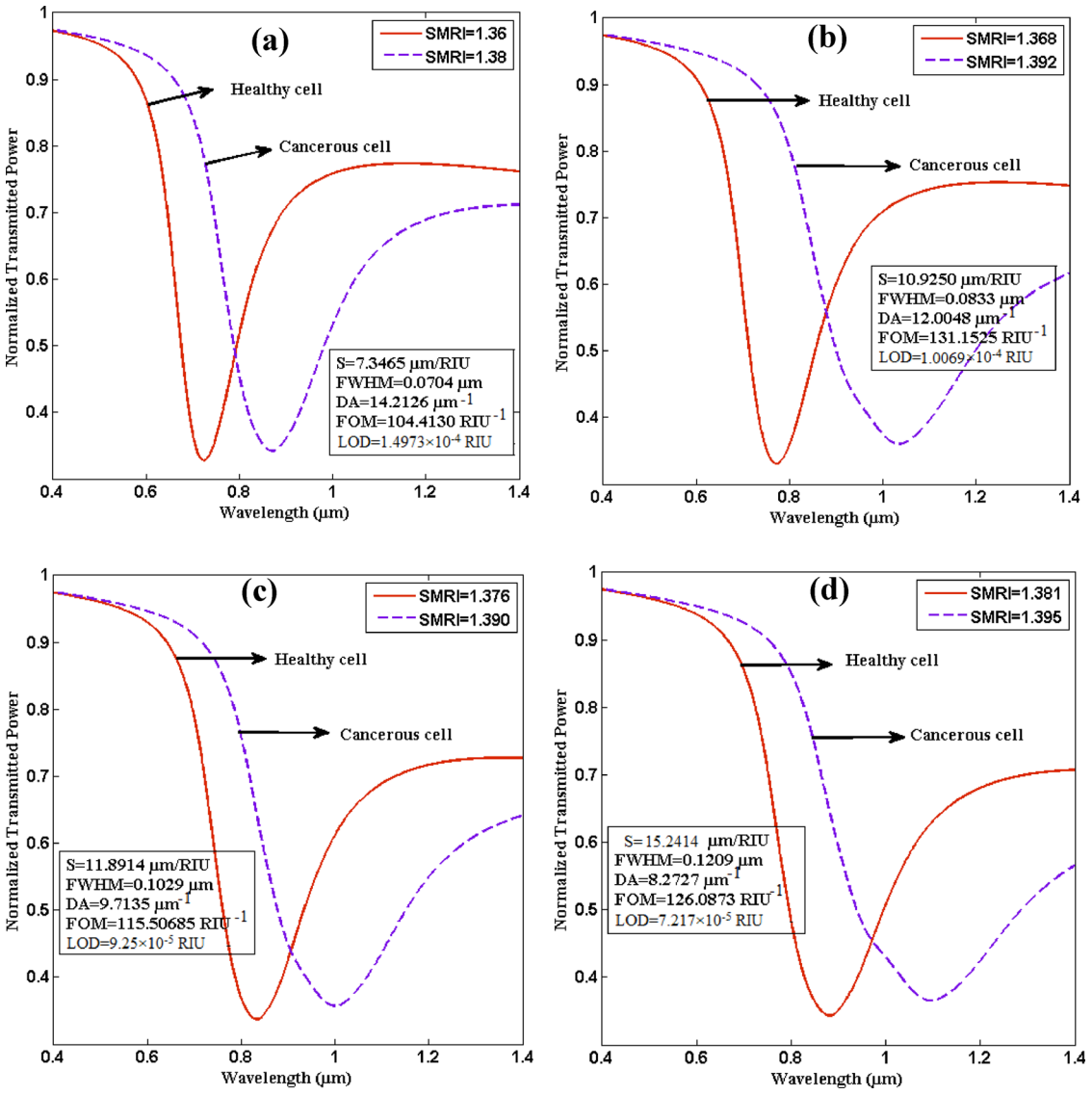

Figure 10. Transmitted SPR curves for the detection of (a) Basal cells, (b) HeLa cells, (c) Jurkat cells, and (d) PC12 cells.

Table 2. Performance Analysis of the Proposed Tapered Fiber Optic SPR Biosensor for the Detection of Basal, HeLa, Jurkat, and PC12 Cancerous Cells

type of cancer	cell name	sensitivity (μm/RIU)	FWHM (μm)	DA (μm^{-1})	FOM (RIU^{-1})	LOD (RIU)
skin	Basal	7.3465	0.0704	14.2126	104.4130	1.4973×10^{-4}
cervical	HeLa	10.9250	0.0833	12.0048	131.1525	1.0069×10^{-4}
blood	Jurkat	11.8914	0.1029	9.7135	115.50685	9.25×10^{-5}
adrenal gland	PC12	15.24114	0.1209	8.2727	126.0873	7.217×10^{-5}

designed sensor configuration. For this, we have chosen four different combinations: $N = 1$ $M = 1$, $N = 1$ $M = 2$, $N = 2$ $M = 1$, and $N = 2$ $M = 2$. Here, 'N' and 'M' stand for the number of graphene and antimonene layers, respectively. The nomenclature of the fiber sensing probe will be as: Au + N * graphene + M * antimonene. Figure 8a–d displays the behavior of sensitivity, FWHM, DA, and FOM, respectively, with the increase in the number of graphene and antimonene overlayers. In Figure 8a, we can see that sensitivity increases with the increase in the number of graphene and antimonene layers, but the enhancement is very small. It means that further increment in 'N' and 'M' becomes insignificant. Similarly, the FWHM increases with the increase in the number of graphene and antimonene monolayers which means that SPR curves become broader as shown in Figure 8b. The maximum FWHM was observed for the combination of $N = 2$ $M = 2$ which is 0.1073 μm then followed by the combination of $N = 1$ $M = 2$, $N = 2$ $M = 1$, and $N = 2$ $M = 2$. On the other hand, DA and FOM decrease if we increase the number of graphene and antimonene overlayers as explained in Figure 8c,d, respectively. Thus, the maximum DA and FOM were observed for $N = 1$ $M = 1$ and minimum for $N = 2$ $M = 2$ combination. At TR 1.0, the highest DA and FOM for $N = 2$ $M = 2$ combination was detected as 16.5893 μm^{-1} and 54.9934 RIU^{-1}, respectively. In the next section, the proposed sensing configuration (Au +

https://doi.org/10.1021/acsomega.2c06037
ACS Omega 2023, 8, 4627−4638

graphene + antimonene) is used for the detection of various cancerous cells such as Basal, HeLa, Jurkat, and PC12.

3.5. Utilization of the Proposed Configuration for the Detection of Cancerous Cells. So far, we have presented only the RI sensing application of the designed fiber sensing configuration. Since healthy and cancerous cells of the same type have different RIs, the proposed fiber optic configuration has been used to differentiate between these cells. Figure 9 displays the combined transmitted SPR curves for the various types of healthy and cancerous cells. It is observed that for a healthy cell, the RWs are obtained at shorter wavelengths and show a red shift for the cancerous cells. Figure 10a–d depicts the transmitted SPR curves for the detection of Basal, HeLa, Jurkat, and PC12 cancerous cells, respectively. Figure 10a displays the transmitted SPR curves for the Basal cell (skin cancer) with a minimum transmittance of 0.7238 and 0.8707 μm for the healthy and cancerous cells, respectively. It means that a 0.1469 μm shift in RW is measured due to cancer-affected Basal cells from the healthy cells. Hence, by adopting this procedure, we can detect cancer present in the Basal cells.

The calculation shows that with the proposed sensing configuration for sensing Basal cells, the sensitivity comes out to be 7.3465 μm/RIU, with an FWHM of 0.0704 μm, a DA of 14.2126 μm^{-1}, an FOM of 104.4130 RIU^{-1}, and an LOD of 1.4973×10^{-4} RIU. Correspondingly, the analysis from Figure 10b–d illustrates that for the detection of HeLa, Jurkat, and PC12 cancerous cells, the RW shows a shift of 0.2622, 0.1665, and 0.2134 μm, respectively. For the detection of cancerous HeLa cells, the highest sensitivity of 10.9250 μm/RIU is achieved with an FWHM of 0.0833 μm, a DA of 12.0048 μm^{-1}, an FOM of 131.1525 RIU^{-1}, and an LOD of 1.0069×10^{-4} RIU. In the same way, the sensitivities for the detection of Jurkat and PC12 cells are achieved as 11.8914 and 15.2414 μm/RIU, respectively. In ref 67, it has been reported that these shifts in the RW may be due to the nature of cell compositions. When a particular cell undergoes transition from healthy to the cancer cell state, it experiences biochemical, physical, and morphological changes.[68] This is due to the variation of its metabolic, genomic, and proteomic properties.[69] These changes affect the RI, resulting in a shift in the RW and allowing them to be distinguished from each other. Furthermore, the cancer cell surface has more negative charge than healthy cells due to the presence of sialic acid residues.[70]Table 2 shows the performance analysis of the proposed tapered fiber optic SPR biosensor for the detection of Basal, HeLa, Jurkat, and PC12 cancerous cells in detail. Thus, it is clear that the maximum sensitivity for the designed configuration comes out to be 15.2414 μm/RIU with a maximum FWHM of 0.1209 μm, a DA of 14.2126 μm^{-1}, an FOM of 131.1525 RIU^{-1}, and an LOD of 7.2×10^{-5} RIU.

4. CONCLUSIONS

In the above study, we designed a graphene-antimonene-coated uniform-waist tapered fiber optic SPR biosensor for its application in RI sensing and for cancerous cell detection. Antimonene and graphene layers greatly enhanced the performance of the designed SPR sensor for sensing cancer analytes. The theoretical analysis was based on the *N*-layer matrix model. The performance of the proposed SPR biosensor was evaluated in terms of its sensitivity, DA, FOM, and LOD. The numerical results showed that the designed sensor was able to provide a sensitivity of 7.3465, 10.9250, 11.8914, and 15.2414 μm/RIU, respectively, for sensing skin, cervical, blood, and adrenal gland cancer with a maximum FOM of 131.1525 RIU^{-1}, a DA of 14.2126 μm^{-1}, and an LOD of 7.2×10^{-5} RIU.

AUTHOR INFORMATION

Corresponding Author

Paola Saccomandi − *Department of Mechanical Engineering, Politecnico di Milano, Milan 20156, Italy;* orcid.org/0000-0003-4236-8033; Email: paola.saccomandi@polimi.it

Author

Vikas − *Department of Mechanical Engineering, Politecnico di Milano, Milan 20156, Italy*

Complete contact information is available at: https://pubs.acs.org/10.1021/acsomega.2c06037

Notes

The authors declare no competing financial interest.

ACKNOWLEDGMENTS

This work was supported by Fondazione Cariplo, grant No. 2017-2075.

REFERENCES

(1) Katz, R.; Edelson, M.*The Cancer-Fighting Kitchen: Nourishing, Big-Flavor Recipes for Cancer Treatment and Recovery*; Ten Speed Press, Crown Publishing Group, 2010.

(2) Cooper, K.; Squires, H.; Carroll, C.; Papaioannou, D.; Booth, A.; Logan, R. F.; Maguire, C.; Hind, D.; Tappenden, P. Chemoprevention of colorectal cancer: systematic review and economic evaluation. *Health Technol. Assess.* **2019**, *14*, 1−206.

(3) *Cancer*, https://www.who.int/news-room/fact-sheets/detail/cancer (accessed October 23, 2021).

(4) Yaroslavsky, A. N.; Patel, R.; Salomatina, E.; Li, C.; Lin, C.; Arashi, M. A.; Neel, V. High contrast mapping of basal cell carcinomas. *Opt. Lett.* **2012**, *37*, 644−646.

(5) Ramer, R.; Hinz, B. Inhibition of cancer cell invasion by cannabinoids via increased expression of tissue inhibitor of matrix metalloproteinases-1. *J. Natl. Cancer Inst.* **2008**, *100*, 59−69.

(6) Jabin, M. A.; Ahmed, K.; Rana, M. J.; Paul, B. M.; Islam, M.; Vigneswaran, D.; Uddin, M. S. Surface plasmon resonance based titanium coated biosensor for cancer cell detection. *IEEE Photon. J.* **2019**, *11*, 1−10.

(7) Mollah, M. A.; Usha, R. J.; Tasnim, S.; Ahmed, K. Detection of cancer affected cell using Sagnac interferometer based photonic crystal fiber refractive index sensor. *Opt. Quant. Electron.* **2020**, *52*, 421.

(8) https://www.cancercenter.com/diagnosing-cancer/lab-tests (accessed October 18, 2020.

(9) Dressing, G. E.; Thomas, P. Identification of membrane progestin receptors in human breast cancer cell lines and biopsies and their potential involvement in breast cancer. *Steroids* **2007**, *72*, 111−116.

(10) Li, T.; Fan, Q.; Liu, T.; Zhu, X.; Zhao, J.; Li, G. Detection of breast cancer cells specially and accurately by an electrochemical method. *Biosens. Bioelectron.* **2010**, *25*, 2686−2689.

(11) Tajima, K.; Obata, Y.; Tamaki, H.; Yoshida, M.; Chen, Y. T.; Scanlan, M. J.; Old, L. J.; Kuwano, H.; Takahashi, T.; Takahashi, T.; Mitsudomi, T. Expression of cancer/testis (CT) antigens in lung cancer. *Lung Cancer* **2003**, *42*, 23−33.

(12) Li, F. R.; Li, Q.; Zhou, H. X.; Qi, H.; Deng, C. Y. Detection of circulating tumor cells in breast cancer with a refined immunomagnetic nanoparticle enriched assay and nested-RT-PCR. *Nanomed.: Nanotechnol., Biol. Med.* **2013**, *9*, 1106−1113.

(13) Glunde, K.; Bhujwalla, Z. M. Metabolic tumor imaging using magnetic resonance spectroscopy. *Semin. Oncol.* **2011**, *38*, 26−41.
(14) Liu, S.; Li, L.; Chen, Z.; Chen, N.; Dai, Z.; Huang, J.; Lu, B. Surface-enhanced Raman spectroscopy measurement of cancerous cells with optical fiber sensor. *Chin. Opt. Lett.* **2014**, *12*, No. S13001.
(15) Hajba, L.; Guttman, A. Circulating tumor-cell detection and capture using microfluidic devices. *TrAC Trends Anal. Chem.* **2014**, *59*, 9−16.
(16) Ahmad, M. A.; Najar, A.; Moutaouakil, A. E.; Nasir, N.; Hussein, M.; Raji, S.; Alnaqbi, A. H. Label-free cancer cells detection using optical sensors. *IEEE Access* **2018**, *6*, 55807−55814.
(17) Ramanujam, N. R.; Amiri, I. S.; Taya, S. A.; Olyaee, S.; Udaiyakumar, R.; Pandian, A. P.; Wilson, K. J.; Mahalakshmi, P.; Yupapin, P. P. Enhanced sensitivity of cancer cell using one dimensional nanocomposite material coated photonic crystal. *Microsyst. Technol.* **2019**, *25*, 189−196.
(18) Sani, M. H.; Khosroabadi, S. A novel design and analysis of high-sensitivity biosensor based on nano-cavity for detection of blood component, diabetes, cancer and glucose concentration. *IEEE Sens.* **2020**, *20*, 7161−7168.
(19) Yasli, A. Cancer detection with surface plasmon resonance-based photonic crystal fiber biosensor. *Plasmonics* **2021**, *16*, 1605−1612.
(20) Arregui, F. J.; Matias, I. R.; Goicoechea, J.; Villar, I. D.Optical fiber sensors based on nanostructured materials. In *Sensors Based on Nanostructured Materials*, Arregui, F. J., Ed.; Springer: Berlin, Heidelberg, 2009; pp. 275−301.
(21) Matias, I. R.; Ikezawa, S.; Corres, J.*Fiber optic sensors: current status and future possibilities*, 1st ed.; Springer International Publishing: Switzerland, 2017).
(22) Wei, L.; Tjin, S. C. Special Issue: Fiber Optic Sensors and Applications: An Overview. *Sensors* **2020**, *20*, 3400.
(23) Bianchi, L.; Mooney, R.; Cornejo, Y.; Hyde, C.; Schena, E.; Berlin, J. M.; Aboody, K.; Saccomandi, P. Fiber Bragg grating sensors-based thermometry of gold nanorod-enhanced photothermal therapy in tumor model. *IEEE Sens. J.* **2021**, *22*, 11297−11306.
(24) Bianchi, L.; Korganbayev, S.; Orrico, A.; Landro, M. D.; Saccomandi, P. Quasi-distributed fiber optic sensor-based control system for interstitial laser ablation of tissue: theoretical and experimental investigations. *Biomed. Opt. Exp.* **2021**, *12*, 2841−2858.
(25) Korganbayev, S.; Landro, M. D.; Wolf, A.; Tosi, D.; Saccomandi, P. Tilted Fiber Bragg grating measurements during laser ablation of hepatic tissues: quasi-distributed temperature reconstruction and cladding mode resonances analysis. *IEEE Sens. J.* **2022**, *22*, 15999−16007.
(26) Lee, B.; Roh, S.; Park, J. Current status of micro- and nano-structured optical fiber sensors. *Opt. Fiber Technol.* **2009**, *15*, 209−221.
(27) Cusano, A.; Lpez-Higuera, J. M.; Matias, I. R.; Culshaw, B. Editorial optical fiber sensor technology and applications. *IEEE Sens. J.* **2008**, *8*, 1052−1054.
(28) Gentleman, D. J.; Obando, L. A.; Masson, J. F.; Holloway, J. R.; Booksh, K. S. Calibration of fiber optic based surface plasmon resonance sensors in aqueous systems. *Anal. Chim. Acta* **2004**, *515*, 291−302.
(29) Sharma, A. K.; Jha, R.; Gupta, B. D. Fiber-Optic Sensors Based on Surface Plasmon Resonance: A Comprehensive Review. *IEEE Sens. J.* **2007**, *7*, 1118−1129.
(30) Vikas; Gupta, S.; Tejavath, K.; Verma, R. K. Urea detection using bio-synthesized gold nanoparticles: an SPR/LSPR based sensing approach realized on optical fiber. *Opt. Quant. Electron.* **2020**, *52*, 278.
(31) Vikas; Yadav, M. K.; Kumar, P.; Verma, R. K. Detection of adulteration in pure honey utilizing Ag-graphene oxide coated fiber optic SPR probes. *Food Chem.* **2020**, *332*, No. 127346.
(32) Kretschmann, E.; Raether, H. Radiative decay of non-radiative surface plasmons excited by light. *Z. Naturforsch.* **1968**, *23*, 2135−2136.
(33) Piliarik, M.; Homola, J.; Maníková, Z.; Čtyroký, J. Surface plasmon resonance sensor based on a single-mode polarization-maintaining optical fiber. *Sens. Actuators B Chem.* **2003**, *90*, 236−242.
(34) Lin, W. B.; Renault, N. J.; Gagnaire, A.; Gagnaire, H. Effects of polarization of the incident light-modeling and analysis of a SPR multimode optical fiber sensor. *Sens. Actuators A Phys.* **2000**, *84*, 198−204.
(35) Verma, R. K.; Gupta, B. D. Theoretical modelling of a bi-dimensional U-shaped surface plasmon resonance based fibre optic sensor for sensitivity enhancement. *J. Phys. D: Appl. Phys.* **2008**, *41*, No. 095106.
(36) Wang, S. F.; Chiu, M. H.; Hsu, J. C.; Chang, R. S.; Wang, F. T. Theoretical analysis and experimental evaluation of D-type optical fiber sensor with a thin gold film. *Opt. Commun.* **2005**, *253*, 283−289.
(37) Vikas; Verma, R. K. Sensitivity enhancement of a lossy mode resonance based tapered fiber optic sensor with an optimum taper profile. *J. Phys. D: Appl. Phys.* **2018**, *51*, 415302.
(38) Ma, Y.; Farrell, G.; Semenova, Y.; Chan, H. P.; Zhang, H.; Wu, Q. Sensitivity enhancement for a multimode fiber sensor with an axisymmetric metal grating layer. *Photon. Nanostruct. Fundam. Appl.* **2014**, *12*, 69−74.
(39) Huang, Y.; Wu, D.; Chuang, C. J.; Nie, B.; Cui, H.; Yun, W. Theoretical analysis of tapered fiber optic surface plasmon resonance sensor for voltage sensitivity. *Opt. Fiber Technol.* **2015**, *22*, 42−45.
(40) Kim, Y. C.; Peng, W.; Banerji, S.; Booksh, K. S. Tapered fiber optic surface plasmon resonance sensor for analyses of vapor and liquid phases. *Opt. Lett.* **2005**, *30*, 2218.
(41) Verma, R. K.; Sharma, A. K.; Gupta, B. D. Surface plasmon resonance based tapered fiber optic sensor with different taper profiles. *Opt. Commun.* **2008**, *281*, 1486−1491.
(42) Vikas; Verma, R. K. On the application of few layer Ti3C2 MXene on fiber optic SPR sensor for performance enhancement. *Eur. Phys. J. D* **2021**, *75*, 5.
(43) Zhou, J.; Yang, T.; Chen, J.; Wang, C.; Zhang, H.; Shao, Y. Two-dimensional nanomaterials-based plasmonic sensing applications: Advances and challenges. *Coord. Chem. Rev.* **2020**, *410*, No. 213218.
(44) Tang, Q.; Zhou, Z. Graphene-analogous low dimensional materials. *Prog. Mater. Sci.* **2013**, *58*, 1244−1315.
(45) Novoselov, A. K. G. K.; Morozov, D. J. S. V.; Zhang, A. A. F. Y.; Dubonos, S.; Grigorieva, I. V. Electric field effect in atomically thin carbon films. *Science* **2004**, *306*, 666−669.
(46) Elias, D. C.; Gorbachev, R. V.; Mayorov, A. S.; Morozov, S. V.; Zhukov, A. A.; Blake, P.; Ponomarenko, L. A.; Grigorieva, I. V.; Novoselov, K. S.; Guinea, F.; Geim, A. K. Dirac cones reshaped by interaction effects in suspended graphene. *Nat. Phys.* **2011**, *7*, 701−704.
(47) Geim, A. K.; Novoselov, K. S. The rise of graphene. *Nanosci. Nanotechnol.* **2010**, 11−19.
(48) Maharana, P. K.; Srivastava, T.; Jha, R. Low index dielectric mediated surface plasmon resonance sensor based on graphene for near infrared measurements. *J. Phys. D: Appl. Phys.* **2014**, *47*, No. 385102.
(49) Verma, A.; Prakash, A.; Tripathi, R. Sensitivity enhancement of surface plasmon resonance biosensor using graphene and air gap. *Opt. Commun.* **2015**, *357*, 106−112.
(50) Farmani, A.; Soroosh, M.; Mozaffari, M. H.; Daghooghi, T.Chapter 25- Optical nanosensors for cancer and virus detections. In *Nanosensors for Smart Cities*; Elsevier: 2020; pp. 419 −432.
(51) Farmani, H.; Farmani, A. Graphene sensing nanostructure for exact graphene layers indentification at tetraheartz frequency. *Phys. E: Low-Dimens. Syst. Nanostruct.* **2020**, *124*, No. 114375.
(52) Moradiani, M.; Farmani, A.; Yavarian, M.; Mir, A.; Behzadfar, F. A multimode graphene plasmonic perfect absorber at tetrahertx frequencies. *Phys. E: Low-Dimens. Syst. Nanostruct.* **2020**, *122*, No. 114159.
(53) Amoosoltani, N.; Mehrabi, K.; Zarifkar, A.; Farmani, A.; Yasrebi, N. Double-Ring resonator plamonic refractive index sensor

https://doi.org/10.1021/acsomega.2c06037
ACS Omega 2023, 8, 4627−4638

utilizing dual-band unidirectional reflectionless propagation effect. *Plamonics* **2021**, *16*, 1277−1285.
(54) Pizzi, G.; Gibertini, M.; Dib, E.; Marzari, N.; Lannaccone, G.; Fiori, G. Performance of arsenene and antimonene double-gate MOSFETs from first principles. *Nat. Commun.* **2016**, *7*, 12585.
(55) Xue, T.; Liang, W.; Li, Y.; Sun, Y.; Xiang, Y.; Zhang, Y.; Dai, Z.; Duo, Y.; Wu, L.; Qi, K.; Shivananju, B. N.; Zhang, L.; Cui, X.; Zhang, H.; Bao, Q. Ultrasensitive detection of miRNA with an antimonene-based surface plasmon resonance sensor. *Nat. Commun.* **2019**, *10*, 28.
(56) Singh, M. K.; Pal, S.; Verma, A.; Das, R.; Prajapati, Y. K. A nanolayered structure for sensitive detection of hemoglobin concentration using surface plasmon resonance sensor. *Appl. Phys. A: Mater. Sci. Process.* **2021**, *127*, 832.
(57) Birks, T. A.; Li, Y. W. The Shape of Fiber Tapers. *J. Light Technol.* **1992**, *10*, 432−438.
(58) Sharma, A. K.; Gupta, B. D. On the performance of different bimetallic combinations in surface plasmon resonance based fiber optic sensors. *J. Appl. Phys.* **2007**, *101*, No. 093111.
(59) Snyder, A. W.; Love, J.*Optical Waveguide Theory*; Springer Science and business media, 2012.
(60) Vikas; Verma, R. K. Design considerations of a surface plasmon resonance (SPR) based tapered fiber optic bio-sensing probe with graphene-MoS_2 over layers. *Optik* **2019**, *180*, 330−343.
(61) Mishra, A. K.; Mishra, S. K.; Verma, R. K. Graphene and beyond Graphene MoS_2: A new window in surface-plasmon-resonance-based fiber optic sensing. *J. Phys. Chem. C* **2016**, *120*, 2893−2900.
(62) Ares, P.; Zamora, F.; Herrero, J. G. Optical identification of few layer antimonene crystals. *ACS Photonics* **2017**, *4*, 600−605.
(63) Lv, H.; Zhang, K.; Ma, X.; Zhong, W.; Wang, Y.; Gao, X. Optimum design of the surface plasmon resonance sensor based on polymethyl methacrylate fiber. *Phys. Open* **2021**, *6*, No. 100054.
(64) Salihoglu; Balci, S.; Kocabas, C. Plasmon-polaritons on graphene-metal surface and their use in biosensors. *Appl. Phys. Lett.* **2012**, *100*, 213110.
(65) Chen, S.; Liu, T.; Guo, J. Optical phase-shift detection of surface plasmon resonance. *Appl. Opt.* **1998**, *37*, 1747.
(66) Choi, S. H.; Kim, Y. L.; Byun, K. M. Graphene-on-silver substrates for sensitive surface plasmon resonance imaging biosensors. *Opt. Express* **2011**, *19*, 458−466.
(67) Jacques, S. L. Optical properties of biological tissues: A review. *Phys. Med. Biol.* **2013**, *58*, R37.
(68) Lodish, H.; Berk, A.; Zipursky, S. L.; Matsudaira, P.; Baltimore, D.; Darnell, J.*Molecular Cell Biology*; W.H. Freeman: New York, NY, USA, 2000.
(69) Yuan, L. W.; Yamashita, H.; Seto, Y. Glucose metabolism in gastric cancer: The cutting-edge. *World J. Gastroenterol.* **2016**, *22*, 2046.
(70) Chen, B.; Le, W.; Wang, Y.; Li, Z.; Wang, D.; Ren, L.; Lin, L.; Cui, S.; Hu, J. J.; Hu, Y.; Yang, P.; Ewing, R. C.; Shi, D.; Cui, Z. Targeting negative surface charges of cancer cells by multifunctional nanoprobes. *Theranostics* **2016**, *6*, 1887−1898.

https://doi.org/10.1021/acsomega.2c06037
ACS Omega 2023, 8, 4627−4638